

# Improvement of Torque Capability of Permanent-Magnet Motor by Using Hybrid Rotor Configuration

Guohai Liu, *Senior Member, IEEE*, Gaohong Xu, Wenxiang Zhao, *Senior Member, IEEE*, Xinxin Du, and Qian Chen, *Member, IEEE*

**Abstract**—This paper proposes a novel hybrid rotor permanent-magnet (HRPM) motor to improve torque capability, including average torque and torque ripple. The key of the proposed motor is that it can utilize high PM torque of surface-inserted PM (SPM) rotor module and high reluctance torque of interior PM (IPM) rotor module at the same time. Meanwhile, the shifting angle of SPMs and open angle of air barriers are introduced to improve the average torque and reduce the torque ripple, respectively. The two variables are employed to create circumferential asymmetry of the rotor for generating an angular difference of the electromagnetic torque between adjacent N-pole and S-pole, thus minimizing torque ripple. In order to evaluate the proposed motor, an IPM motor and a SPM motor with the same dimension and volume of PM are used as benchmarks. Through theoretical analysis and experimental test, it is verified that the proposed HRPM motor can offer higher torque density and lower torque ripple simultaneously.

**Index Terms**—Asymmetric rotor, hybrid rotor, permanent-magnet (PM) motor, torque, torque ripple.

## I. INTRODUCTION

**D**UE to the ever-increasing concerns about the energy crisis and environmental pollution, electric vehicles (EVs) and hybrid EVs (HEVs) have been researched extensively [1]. As one of the key technologies for EVs and HEVs, the design of their motors is greatly fundamental. Given this, various types of electric motors have been proposed, among which the permanent-magnet (PM) brushless motor has been paid great attention because of high torque density, high power density and

high efficiency [2], [3]. Generally, PM brushless motors can be classified as surface PM (SPM) ones and interior PM (IPM) ones [4], [5]. The SPM motors have higher PM torque density because their PMs are more close to air-gap [6], [7]. However, the SPM motors offer insignificant reluctance torque, suffering from the low flux-weakening capacity [8]. The IPM motors offer the advantages, such as high torque density and high efficiency, as well as extended speed range, benefitting from both PM torque and reluctance torque [9], [10]. Furthermore, the V-type IPM motor contains higher saliency ratio and lower PM losses than the flat type one, which is more suitable for high-speed applications, and has been employed from Prius 2004 to Prius 2010 [11], [12]. In order to replace V-type IPM motor, many candidates have been proposed. The flux-switching PM motor can offer high PM torque, which result in similar torque density to V-type IPM motor, but its utilization ratio of PM material is relatively low [13], [14]. The spoke-type PM motor has high PM material utilization ratio, but the mechanical robustness is poor because of the split rotor configuration [15], [16]. Considering the high cost and unstable availability of rare-earth PM, the ferrite PM-assisted synchronous reluctance motor has been considered to replace V-type IPM motor [17], [18]. Meanwhile, a switched reluctance motor has been developed as one of the possible low cost candidates [19]–[21]. Although these candidates offer inherent advantages compared with V-type IPM motor, their torque capabilities, including average torque and torque ripple, should be improved further.

In order to increase the average torque, the third harmonic current was injected into the PM motor [22], [23]. Recently, a novel V-type motor with assisted barriers between two adjacent poles was proposed, in which the current phase angle of the maximum PM torque were adjusted to be same with that of the maximum reluctance torque [24], [25]. Although it is an interesting way to improve average torque, it should be noticed that the PM torque or reluctance torque of these IPM motors are relatively low because of larger air barrier of adjacent poles. Meanwhile, the torque ripple is relatively severe.

Generally, there are three main designing strategies for torque ripple reduction, involving stator, winding and rotor. Firstly, skewing of stator slots or PMs is a well-known method to reduce torque ripple. However, this method has difficulties in manufacturing and thus increases the motor cost [26].

Manuscript received July 26, 2016; revised November 24, 2016; accepted January 25, 2017. Date of publication February 8, 2017; date of current version August 18, 2017. This work was supported in part by the National Natural Science Foundation of China under Grant 51577084 and Grant 51422702, by the China Postdoctoral Science Foundation under Grant 2016M591782, by the Research Fund for the 333 Project of Jiangsu Province under Grant BRA2015302, by the Natural Science Foundation of Jiangsu Province under Grant BK20160518, by the Key Project of Natural Science Foundation of Jiangsu Higher Education Institutions under Grant 15KJA470002, by the Graduate Education Innovation Project of Jiangsu Province under Grant KYLX15\_1083, and by the Priority Academic Program Development of Jiangsu Higher Education Institutions. Paper no. TEC-00628-2016. (Corresponding author: W. Zhao.)

The authors are with School of Electrical and Information Engineering, Jiangsu University, Zhenjiang 212013, China, and also with the Jiangsu Key Laboratory of Drive and Intelligent Control for Electric Vehicle, Zhenjiang 212013, China (e-mail: ghliu@ujs.edu.cn; xugaohongujs@163.com; zwx@ujs.edu.cn; 2285485872@qq.com; chenqian0501@ujs.edu.cn).

Color versions of one or more of the figures in this paper are available online at <http://ieeexplore.ieee.org>.

Digital Object Identifier 10.1109/TEC.2017.2665686

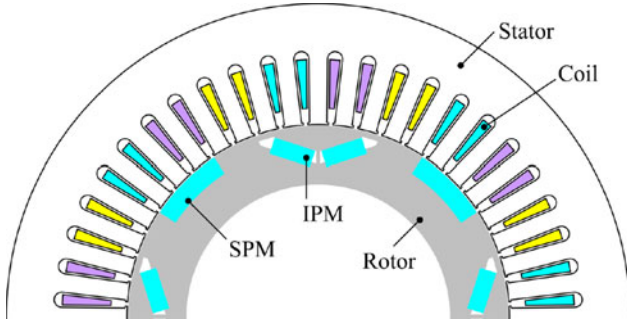


Fig. 1. HRPM motor (initial model).

Secondly, fractional-slot windings can be used to produce various stator magnetomotive force harmonics for minimum torque ripple [27], but this technique is more suitable for double layer windings. Thirdly, due to the merits like simplicity, effectiveness as stepping skewing and low cost in manufacturing, magnet shifting is an extensively applied method for torque ripple reduction [28]. However, the reduction of torque ripple always results in a slight loss of average torque [29].

In this paper, a hybrid rotor permanent-magnet (HRPM) motor with asymmetric rotor configuration is proposed, which achieves significant improvement of average torque as well as reduction of torque ripple simultaneously. The hybrid rotor is composed of IPM rotor modules and SPM rotor modules, which generate high reluctance torque and high PM torque, respectively. The shifting angle of SPMs and open angle of air barriers are designed to improve the torque capability. The motor structure and features will be given in Section II. In Section III, the proposed HRPM motor will be designed and analyzed. In Section IV, the electromagnetic performances of HRPM motor will be compared and evaluated with IPM and SPM motors. The experimental test will be offered in Section V. Finally, some conclusions will be drawn in Section VI.

## II. TOPOLOGY AND FEATURES

Fig. 1 shows the cross section of the newly proposed HRPM motor. The stator has 48 slots with integral slot distributed windings, and the rotor is composed of two different rotor modules with 8 poles. It can be observed that there are two kinds of rare-earth PMs, the SPMs and IPMs are adjacently located in the rotor. The reason to adopt the IPM rotor module is that it can produce high reluctance torque. Meanwhile, the SPM rotor module can be seen as the rotor of the switched reluctance motor with inset PMs. Thus, it will not only retain a certain reluctance torque but also enhance PM torque. Hence, taking both the reluctance and PM torque contributions into consideration, the aforementioned two rotor modules are chosen to build a hybrid rotor. Then, the average torque of the HRPM motor can be guaranteed. Benefiting from the adoption of the SPMs, the shifting angle of SPMs and the open angle of the air barriers beside the SPM along the circumference of the rotor can be designed to improve the torque capability, including average torque and torque ripple.

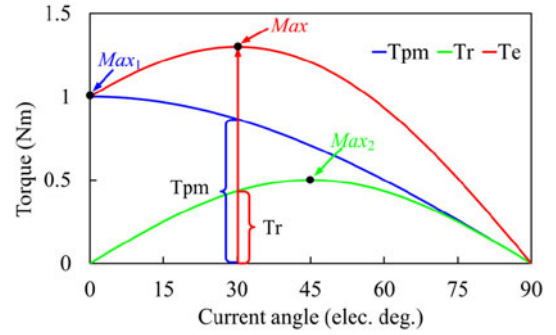


Fig. 2. Torque versus current angle of HRPM motor.

The electromagnetic torque of the HRPM motor in the  $d$ - $q$  rotating reference can be expressed as:

$$\begin{aligned} T_e &= \frac{3P}{2} [\psi_{pm} i_q + (L_d - L_q) i_d i_q] \\ &= \frac{3P}{2} \left[ \psi_{pm} I_a \cos \beta + \frac{1}{2} (L_d - L_q) I_a^2 \sin 2\beta \right] \\ &= T_{pm} + T_r \end{aligned} \quad (1)$$

where  $P$  is the number of pole pairs,  $L_d$  and  $L_q$  are the inductances of the  $d$ - and  $q$ -axes, respectively,  $i_d$  and  $i_q$  are the currents of the  $d$ - and  $q$ -axes, respectively,  $\psi_{pm}$  is the PM flux linkage,  $I_a$  is the peak value of the phase current and  $\beta$  is the current angle which is spatial angle of the stator current vector measured with respect to the  $q$ -axis,  $T_e$  is the output electromagnetic torque,  $T_{pm}$  and  $T_r$  are the PM torque and reluctance torque, respectively.

Equation (1) reveals that the output torque contains two components. The first one is the  $T_{pm}$ , which is produced by the interaction between  $\psi_{pm}$  and  $i_q$ , and the second one is the  $T_r$  owing to the rotor saliency ( $L_d - L_q$ ). Fig. 2 illustrates the relationship between the torque components and current angle based on (1), it can be seen that both the torque components do not have full utilization rate of their maximum values.

## III. MOTOR DESIGN

In order to analyze the relationship among shifting angle of SPMs, open angle of air barriers and electromagnetic performances of the proposed HRPM motor, the time-stepping finite-element method (FEM) is employed.

### A. Effect of Shifting Angle of SPMs on Average Torque

The shifting angle  $\theta_1$  of SPMs is shown in Fig. 3. After the SPMs are shifted along the circumference of the rotor, the rotor is asymmetric and the torque performance of HRPM motor will be changed, which is investigated in Fig. 4. Fig. 4(a) gives the torque-angle performance, showing that the torque changes obviously when the SPMs are shifted. As shown in Fig. 4(b), the torque at the current angle of  $0^\circ$  decreases with increasing  $\theta_1$ . On the contrary, the torque at the current angle of  $90^\circ$  increases with increasing  $\theta_1$  as shown in Fig. 4(c). As shown in

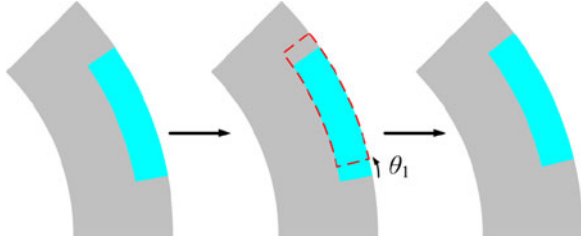


Fig. 3. Shifting angle of SPM.

Fig. 4(d), the maximum average torque increases for the overall trend as  $\theta_1$  increasing from  $-4^\circ$  to  $3^\circ$ , though it does not change linearly. Nevertheless, the maximum average torque decreases significantly when  $\theta_1$  varies from  $3^\circ$  to  $4^\circ$ . Finally, the optimized  $\theta_1$  is chosen as  $3^\circ$  for the further optimization.

### B. Effect of Open Angle of Air Barriers on Torque Ripple

Torque ripple is also a serious concern in HRPm motor because it is relatively high. In the HRPm motor, the shifting of SPMs can achieve improvement of average torque, and the employment of air barriers is used to obtain reduction of torque ripple.

Fig. 5 shows the open angle  $\theta_2$  of air barrier. In Fig. 6, the effect of open angle of air barriers on torque ripple is investigated. It can be observed that the torque ripple decreases gradually when  $\theta_2$  varies from  $0^\circ$  to  $3^\circ$ . On the contrary, the torque ripple increases with  $\theta_2$  changing from  $3^\circ$  to  $5^\circ$ . Considering the compromise between average torque and torque ripple, the optimized  $\theta_2$  is selected as  $3^\circ$  for the final model.

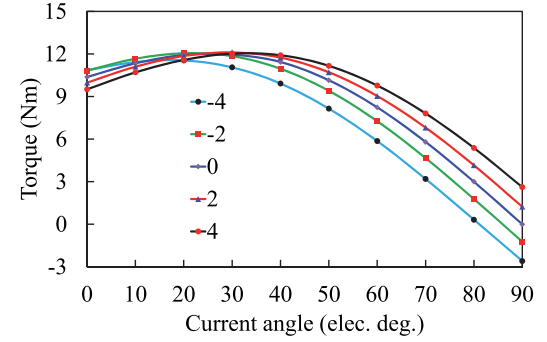
### C. Promotion of Torque Capability

After the optimization and investigation of shifting angle of SPMs and open angle of air barriers, the optimized rotor of HRPm motor is given in Fig. 7. The comparison of instantaneous torque waveforms of HRPm motor, pre and post optimization (termed as initial model and final model), are shown in Fig. 8. Obviously, average torque and torque ripple, which represent the torque capability, have been improved. It should be noted that average torque has been promoted by 5.3% with the same volume of rear-earth PM and the torque ripple is significantly reduced to 10.4%.

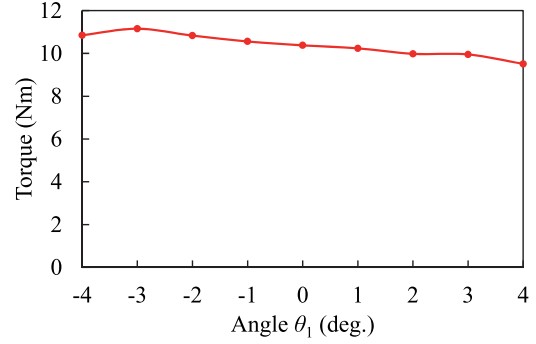
### D. Torque Components

The output average torque is consisted of PM torque and reluctance torque components. Meanwhile, the output average torque is improved after optimization. Hence, it is necessary to find out which torque component is the main promotion for the average torque.

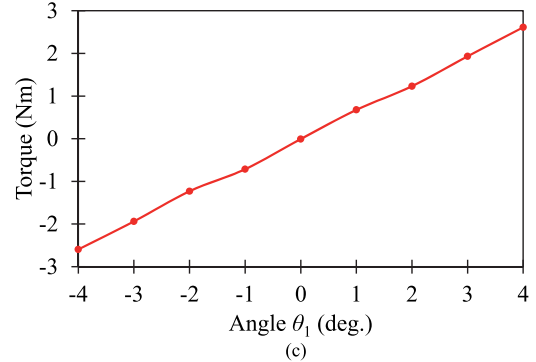
Since  $\Psi_{pm}$  is in direct proportion to no-load back electromotive force  $E_0$  in (2), it is apparent from (3) that the PM torque  $T_{pm}$  is in the same proportion to  $E_0$ . Thus, the  $E_0$  is adopted to replace  $\Psi_{pm}$  in the following analysis, because the  $E_0$  can be



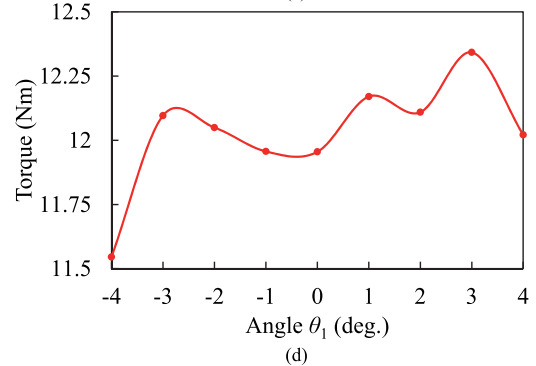
(a)



(b)



(c)



(d)

Fig. 4. Torque performance with shifting of SPMs. (a) Torque-angle performance. (b) Torque at current angle of  $0^\circ$ . (c) Torque at current angle of  $90^\circ$ . (d) Maximum torque.

obtained easily by FEM.

$$E_0 = \omega_r \psi_{pm} \quad (2)$$

$$T_{pm} = \frac{3P}{2} \frac{E_0}{\omega_r} i_q \quad (3)$$

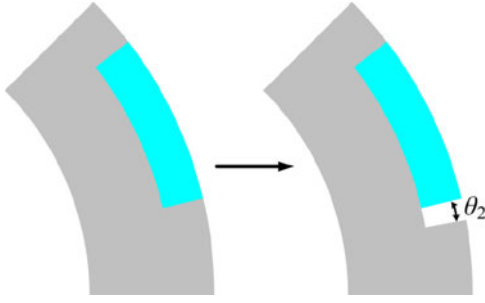


Fig. 5. Open angle of air barrier.

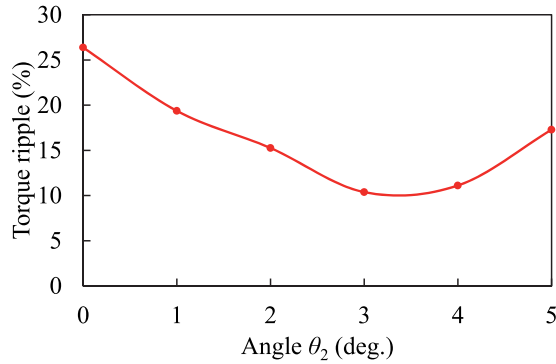


Fig. 6. Torque ripple with shifting of air barriers.

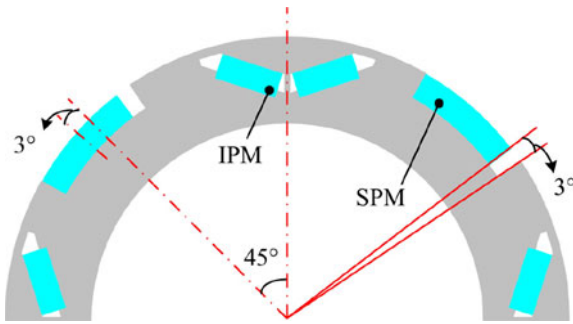


Fig. 7. Rotor of optimized HRPm motor.

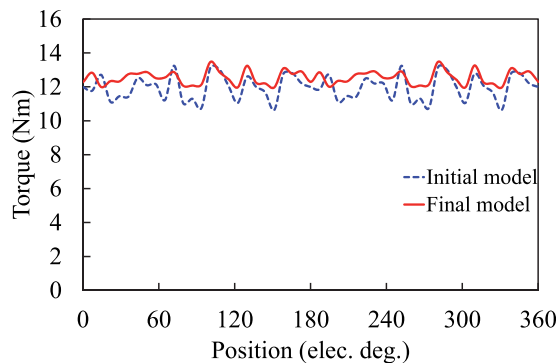
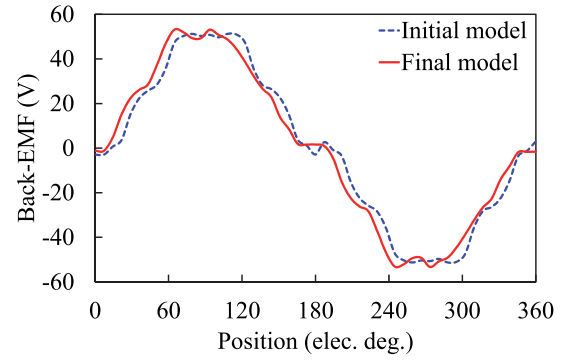
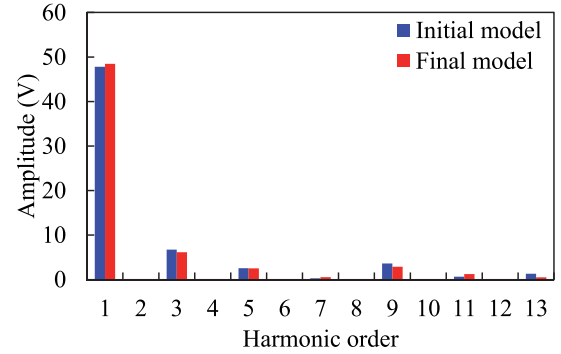


Fig. 8. Instantaneous torque.



(a)



(b)

Fig. 9. No-load performances. (a) Back-EMF. (b) Harmonic orders of back-EMF.

The no-load back-EMFs of the initial and final HRPm motors are shown in Fig. 9(a). It can be seen that the maximum back-EMF value of final model is higher than that of the initial model without additional rear-earth PM material. Additionally, the back-EMF waveform of initial model has distortion at zero crossing, while this phenomenon is not existed in the final model. Fig. 9(b) shows their corresponding harmonic orders. It can be seen that the back-EMF fundamental component of final model is larger, which indicates that the final model of HRPm motor has better utilization of PM material. Furthermore, it is obvious that the back-EMF of final model is less distorted, because the air barriers in final model decrease the flux leakage. Then, more flux linkages of SPMs go into stator core.

The magnitude of reluctance torque can be illustrated by the difference between  $d$ - and  $q$ -axes inductances. As shown in (4), larger reluctance torque is produced by larger  $L_q - L_d$ . The  $L_q$  and  $L_d$  over one electrical cycle of HRPm motor are given in Fig. 10(a). It is shown that both  $L_q$  and  $L_d$  drop after optimization of the rotor. The reduction of  $L_q$  is caused by the enlarged length of  $q$ -axis flux line, while the decrease of  $L_d$  is caused by additional flux barrier in  $d$ -axes flux line. In general, the average value of  $L_q$  is higher than that of  $L_d$ , because the reluctance of  $q$ -axis flux line is relatively smaller than that of  $d$ -axis. The difference between  $L_q$  and  $L_d$  is shown in Fig. 10(b). It can be observed that the final model has the smaller  $L_q - L_d$ , which sacrifices slight reluctance torque for better torque capability. Furthermore, the corresponding torque components of both models are compared in Fig. 11. Although there is a slight decrease in reluctance torque in the final model,



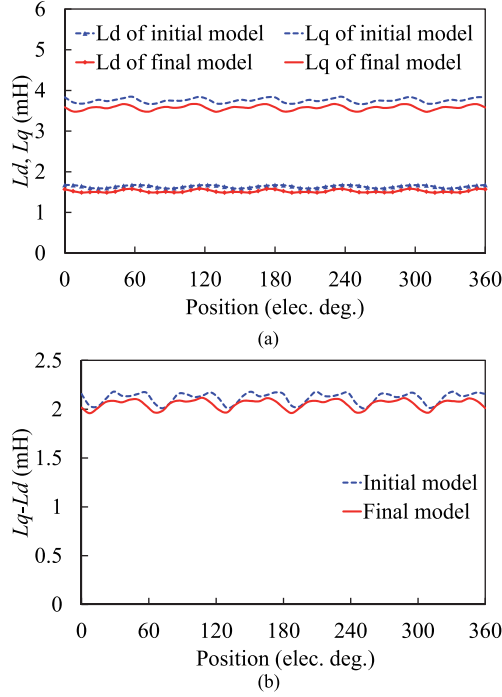


Fig. 10. Inductances of HRPD motor. (a)  $D$ - and  $q$ -axes inductances. (b) Difference between  $L_q$  and  $L_d$ .

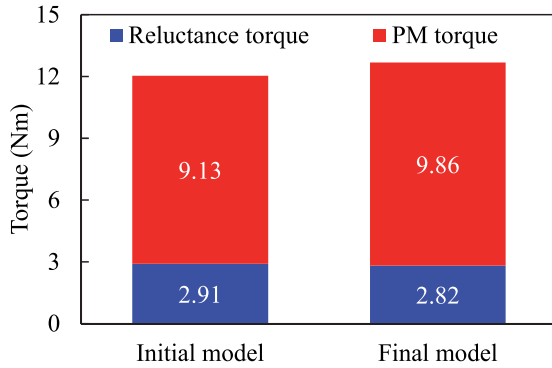


Fig. 11. Torque components.

it is worthwhile to be noted that the promotion of output average torque is mainly contributed by the increase of PM torque.

$$T_r = \frac{3P}{2} (L_d - L_q) i_d i_q \quad (4)$$

#### E. Torque Ripple

In order to explain the significant reduction of torque ripple in the proposed motor with hybrid and asymmetric rotor configuration, the torque of each pole in the final model of HRPD motor is calculated as shown in Fig. 12. It can be seen that there is an angular difference of the torque between the SPM rotor module and the IPM rotor module. Particularly in the red circle area, the position of maximum torque of IPM rotor module is close to that of the minimum torque of SPM rotor module.

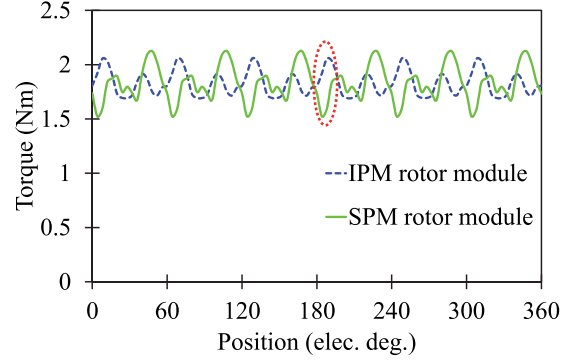


Fig. 12. Torque of adjacent poles in HRPD motor.

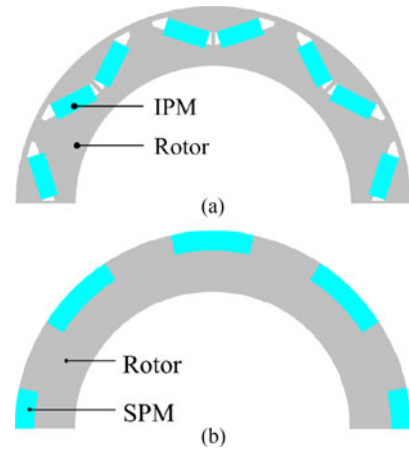


Fig. 13. Rotors of benchmarks. (a) IPM rotor. (b) SPM rotor.

Hence, the torque ripple is greatly reduced when the SPM rotor module and the IPM rotor module are combined together to compose one pole-pair in the HRPD motor. It can be concluded that the proposed HRPD motor can offer higher torque density and lower torque ripple simultaneously.

#### IV. COMPARISON AND EVALUATION

Since the proposed HRPD motor is configured by hybrid SPM rotor modules and IPM rotor modules, an IPM motor and a SPM motor are employed as the benchmarks to illustrate the advantages of the proposed motor. In order to evaluate the proposed motor fairly, the IPM motor and SPM motor are comparatively designed with the same dimensions and volume of PM as HRPD motor. The rotors of the benchmarks are shown in Fig. 13(a) and (b), respectively. Their electromagnetic performances, such as flux distributions, inductances, no-load back-EMFs and torque performances, are calculated and compared.

##### A. Comparisons of Flux Distributions and Inductances

Fig. 14 compares the flux line distributions of the IPM motor, SPM motor and HRPD motor. In the optimized HRPD motor,  $\theta_1$  and  $\theta_2$  are  $3^\circ$  and  $3^\circ$ , respectively.

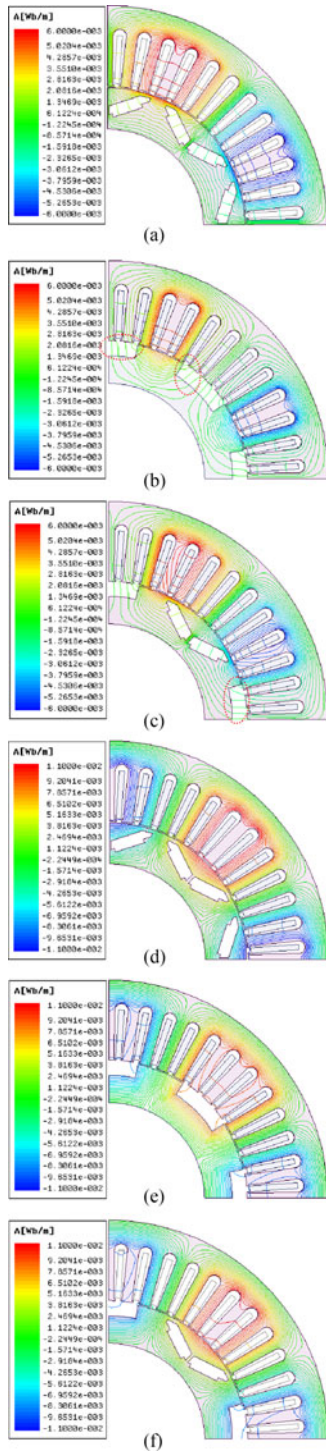


Fig. 14. Flux distributions. (a) IPM motor in  $d$ -axis. (b) SPM motor in  $d$ -axis. (c) HRPM motor in  $d$ -axis. (d) IPM motor in  $q$ -axis. (e) SPM motor in  $q$ -axis. (f) HRPM motor in  $q$ -axis.

The inductances of the IPM motor, SPM motor and HRPM motor are compared in Fig. 15. It can be observed that the IPM motor has higher  $L_d$  and  $L_q$  than the other two motors. Compared with the inductances of IPM motor, the decrease of  $L_d$  of the other two motors is caused by increased flux barrier in  $d$ -axes flux line, which is marked by red circles in Fig. 14. Meanwhile, the reduction of  $L_q$  is caused by the additional

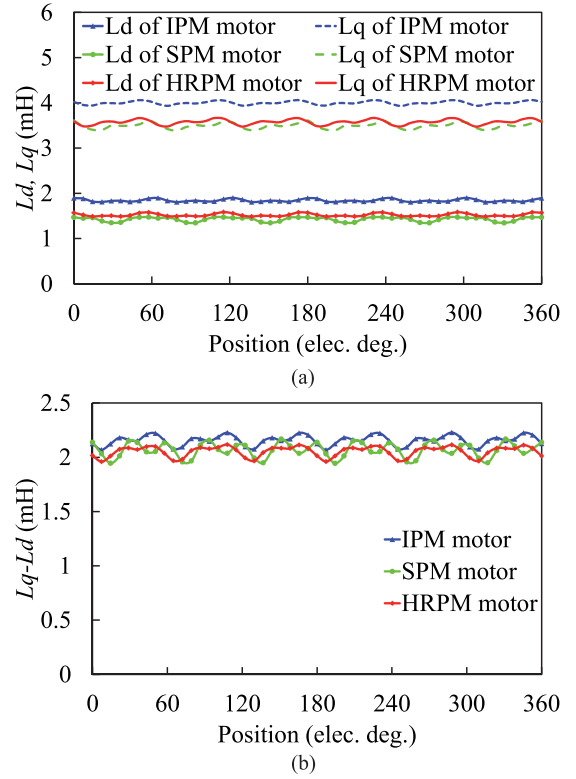


Fig. 15. Inductances. (a)  $D$ - and  $q$ -axes inductances. (b) Difference between  $L_q$  and  $L_d$ .

length of  $q$ -axis flux line. Also, the average value of  $L_q$  is higher than that of  $L_d$  in all motors. The difference between  $L_q$  and  $L_d$  is shown in Fig. 15(b). It can be seen that the IPM motor offers higher difference between  $L_q$  and  $L_d$ , which indicates higher reluctance torque. The average difference between  $L_q$  and  $L_d$  of SPM motor and the optimized HRPM motor are same.

### B. Comparison of Back-EMFs

The comparison of no-load back-EMFs at 1500 r/min is shown in Fig. 16. It can be observed that the maximum value of back-EMF in SPM motor is the highest, followed by the HRPM one and IPM one, successively. Meanwhile, the back-EMF of HRPM motor has asymmetric waveform crest because of the asymmetric rotor configuration. Especially, the waveform of SPM motor has more severe distortion at zero crossing. Fig. 16(b) shows that the amplitude of fundamental component of SPM motor is the highest, which demonstrates that the SPM motor has the best utilization of PM material. However, the harmonic content of SPM motor is the biggest. Benefiting from the employment of SPMs, the back-EMF fundamental component of HRPM motor is much higher than that of IPM motor. Furthermore, it is obvious that the back-EMF of HRPM motor is less distorted than that of the SPM one, because the air barriers restrain a portion of the flux leakage.

### C. Comparison of Torque Performances

Fig. 17 compares the torque performances among the IPM motor, SPM motor and HRPM motor. The corresponding torque

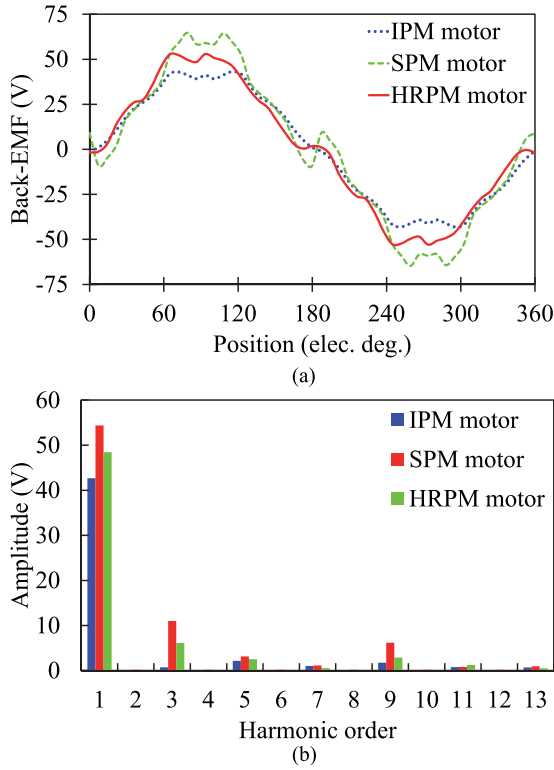


Fig. 16. Comparison of no-load performances. (a) Back-EMF. (b) Harmonic orders of back-EMF.

components of the three motors are shown in Fig. 17(a). It can be observed that the IPM motor offers advantage of the highest reluctance torque, while the SPM motor produces the maximum PM torque. The HRPM motor has higher PM torque than IPM one, but the reluctance torque is comparative to that of SPM motor. The curves of torque-angle performances of the three motors are shown in Fig. 17(b). When the current angle is  $0^\circ$ , the PM torque of the SPM motor is the biggest, which is in agreement with Fig. 17(a). Meanwhile, different from the other two benchmarks, the reluctance torque of the HRPM is larger than zero at the current angle of  $90^\circ$  due to the shifting of PMs and employment of air barriers. Furthermore, the results demonstrate that the torque capability at rated speed of the HRPM motor is significantly improved compared with that of the IPM motor, though it is comparative with the SPM motor.

The torque under maximum-torque-per-ampere (MTPA) operation is shown in Fig. 17(c). It can be observed that the torque ripple of the SPM motor is the highest, and followed by that of the IPM motor. And compared with the IPM motor, the designed HRPM motor achieves 10% higher average torque and 15% smaller torque ripple with the help of hybrid rotor structure and optimized asymmetric rotor configuration. Their cogging torque waveforms are shown in Fig. 17(d). It can be seen that the cogging torque amplitude of the HRPM motor is smaller than that of the IPM and SPM motors.

## V. EXPERIMENTAL VERIFICATION

The designed 48-slot/8-pole HRPM motor is built and tested to verify the theoretical analysis as shown in Fig. 18. It can be

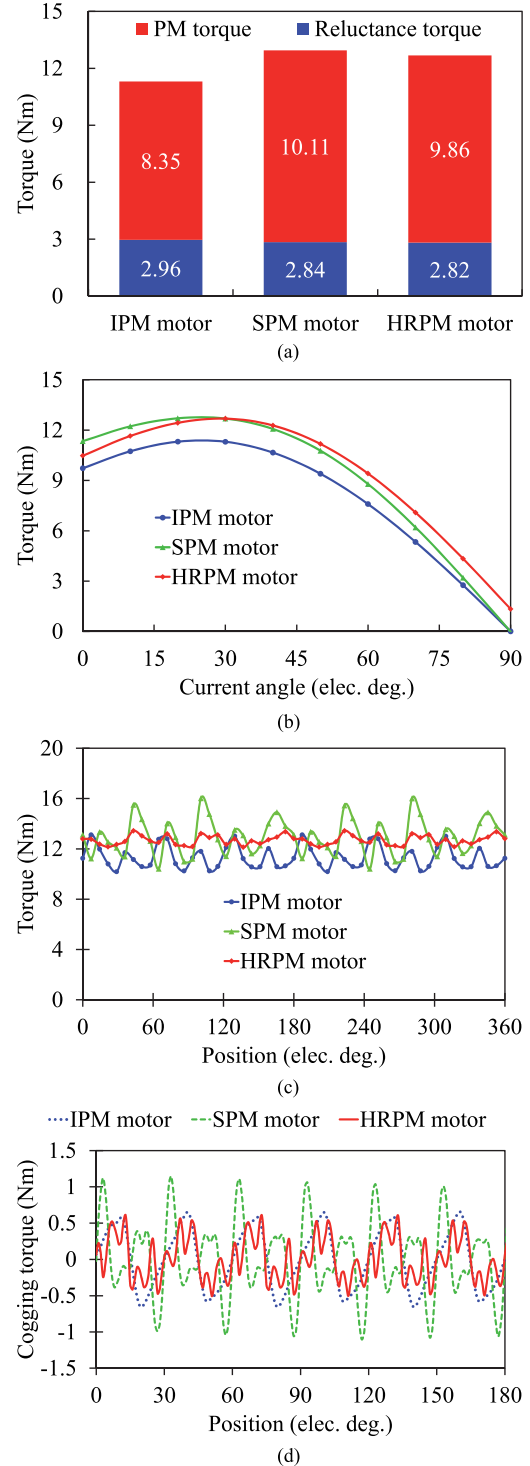


Fig. 17. Torque comparison. (a) Torque components. (b) Torque-angle performance. (c) Torque under MTPA operation. (d) Cogging torque.

seen that the rotor is assembled by four IPM rotor modules and four SPM rotor modules. In order to enhance the robustness of the SPM rotor modules, a peg with stainless steel is employed. The shape of peg is given with red area in Fig. 18, which can be imagined as Z character to reduce the influence of the centrifugal force on SPMs. The key specifications of HRPM motor are summarized in Table I.



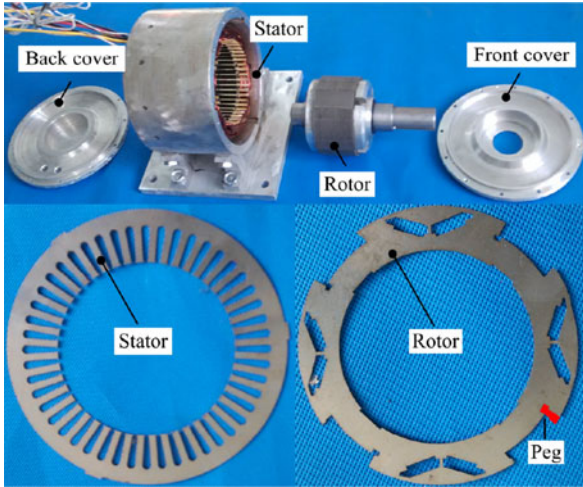


Fig. 18. Prototype motor.

TABLE I  
SPECIFICATIONS OF HRPM MOTOR

| Items                               | HRPM motor |
|-------------------------------------|------------|
| Number of stator slot               | 48         |
| Number of rotor pole                | 8          |
| Rated speed (rpm)                   | 1500       |
| Stack length (mm)                   | 46         |
| Stator outer diameter (mm)          | 155        |
| Stator inner diameter (mm)          | 98         |
| Airgap length (mm)                  | 0.5        |
| Rotor outer diameter (mm)           | 97         |
| Rotor inner diameter (mm)           | 67.7       |
| Total PMs volume (cm <sup>3</sup> ) | 34.6       |
| Number of turns per coil            | 11         |
| Phase resistance at 21 °C (Ω)       | 0.081      |
| Iron core material                  | DW540_50   |
| PM material                         | N35        |
| Remanence of PM (T)                 | 1.23       |
| Coercive force of PM (kA/m)         | −890       |
| Maximum current value (A)           | 23         |

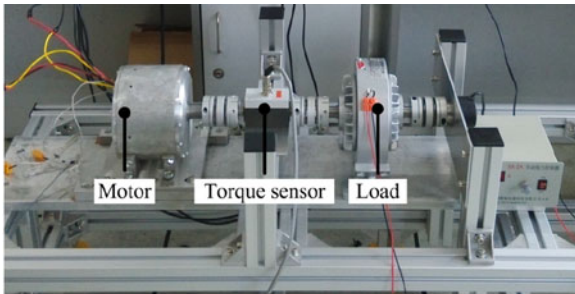


Fig. 19. Experimental platform of HRPM motor drive.

The PM material utilized in this paper is sintered Nd-Fe-B magnets of grade N35 which can offer high energy density at moderate cost.

The experimental platform of the prototype HRPM motor drive is shown in Fig. 19. The digital controller is dSPACE 1103, the intelligent power module is PM100CVA120, the torque

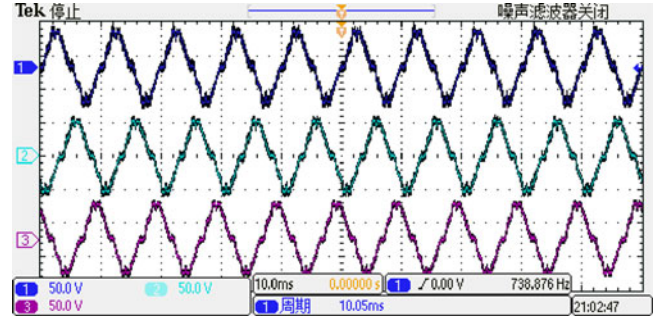


Fig. 20. Measured back-EMFs of HRPM motor at 1500 r/min (10 ms/div, 50 V/div).

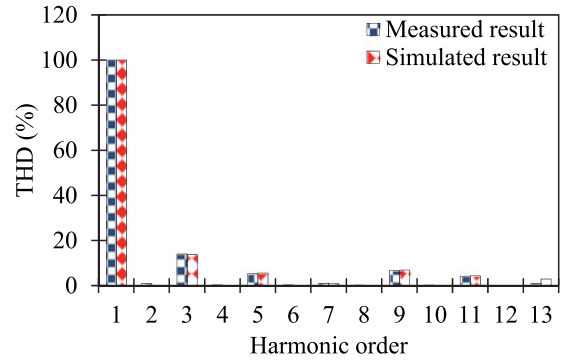


Fig. 21. THD of back-EMF at 1500 r/min.

sensor is HBM T20WN (1 V indicates 2 Nm), the oscilloscope is Tek DPO 2024, and the current sensor is Tek A622 current clamp (0.01 V indicates 1 A). Moreover, a magnetic powder brake is used as load.

The measured phase back-EMF waveforms of the HRPM motor at 1500 r/min are shown in Fig. 20. It can be seen that there is tortuosity at the zero crossing and peak value. By comparing Fig. 20 with Fig. 9, it can be concluded that the measured back-EMF is in good agreement with the simulated one. In order to illustrate it more clearly, the harmonic spectra of the phase back-EMF is given. As shown in Fig. 21, the fundamental value of tested back-EMF is numerically equal to that of FEM results. Moreover, the total harmonic distortion (THD) of the FEM-based back-EMF conforms well to that of the measured one. It can be concluded that the experiment results show the effectiveness of both theoretical analysis and FEM.

Furthermore, the on load performances should also be investigated and tested. Fig. 22 provides the amplitude of injected currents versus loads, in which two commonly used control algorithms including the  $i_d = 0$  control and MTPA control [30] are adopted for different loads. It can be seen that the torque results of both simulated and tested at  $i_d = 0$  control and MTPA control are almost the same before 15 A. This is because the reluctance torque is low when the injected current is lower than 15 A. When the injected current is more than 15 A, the difference of torques at  $i_d = 0$  and MTPA control modes becomes significant. The measured torque under  $i_d = 0$  or MTPA is lower than the simulated one because of the cogging torque. When the load is only cogging torque, the injected current is about 2.5 A.



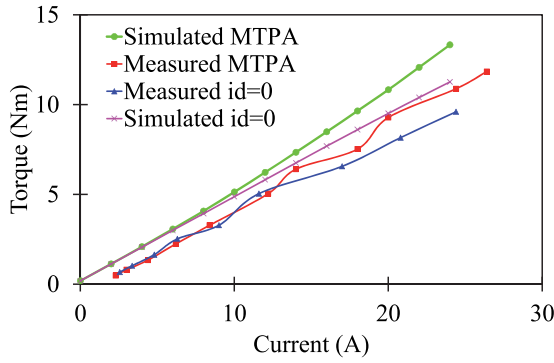


Fig. 22. Torque production versus phase current of the prototype.

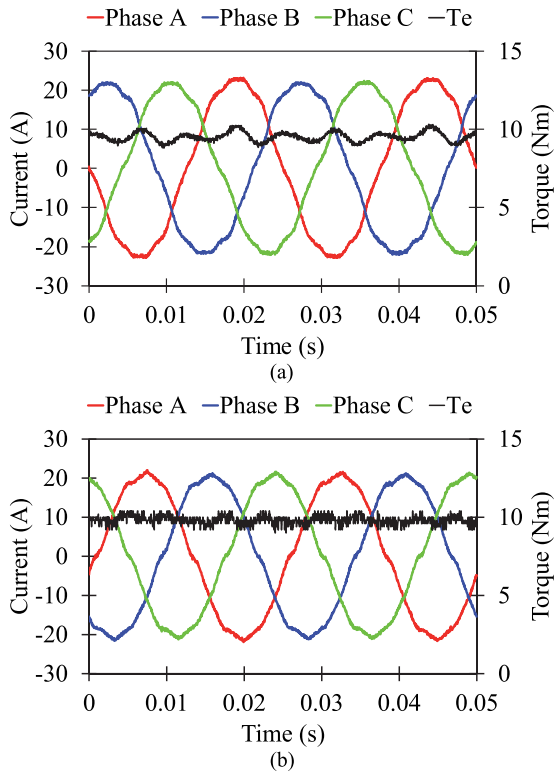


Fig. 23. Measured torque and currents. (a) Sinusoidal voltage injection. (b) SVPWM control method under close-loop.

Meanwhile, there are about 2 A differences between simulated current and measured one. If the difference caused by cogging torque is considered, the measured results are acceptable, which verifies the effectiveness of theoretical analysis and FEM, and the prototype provides good on-load performance.

Since the back-EMF waveforms of the proposed motor are asymmetric, the current and torque ripple are distorted by injected sinusoidal voltage as shown in Fig. 23. In Fig. 23(a), the injected voltage is sinusoidal by keeping smooth voltages of  $d$ - $q$  axes in SVPWM control, it can be seen that the waveforms of the phase currents are distorted because of the asymmetric back-EMF. Then, the torque ripple is about 15.8% which becomes severe than the simulated one (10.4%). In Fig. 23(b), the injected voltage is still produced by SVPWM, but the voltages of  $d$ - $q$  axes are regulated by the close-loop. Then the torque ripple

is about 14.3% though the currents are not sinusoidal. Hence, the torque ripple caused by asymmetric back-EMF can be slightly reduced by SVPWM control method under close-loop.

## VI. CONCLUSION

In this paper, a novel HRPD motor with hybrid rotor has been proposed, which is combined by IPM rotor modules and SPM rotor modules. Meanwhile, benefiting from the novel rotor configuration, the SPMs can be shifted around the rotor circumference to improve the average torque. Furthermore, air barriers are adopted beside the SPMs to produce angular difference of torques between adjacent rotor modules for reducing the high torque ripple. Finally, an IPM motor and a SPM motor with the same dimension and volume of PM are used as benchmarks. From the comparison of electromagnetic performances, such as  $d$ - $q$  inductances, back-EMFs, and torques, the HRPD motor has better torque capability than both the IPM motor and the SPM motor.

## REFERENCES

- [1] R. Cao, C. Mi, and M. Cheng, "Quantitative comparison of flux-switching permanent-magnet motors with interior permanent magnet motor for EV, HEV, and PHEV applications," *IEEE Trans. Magn.*, vol. 48, no. 8, pp. 2374–2384, Aug. 2012.
- [2] Z. Q. Zhu, D. Wu, and X. Ge, "Investigation of voltage distortion in fractional slot interior permanent magnet machines having different slot and pole number combinations," *IEEE Trans. Energy Convers.*, vol. 31, no. 3, pp. 1192–1201, Apr. 2016.
- [3] G. Lei, C. Liu, J. Zhu, and Y. Guo, "Techniques for multilevel design optimization of permanent magnet motors," *IEEE Trans. Energy Convers.*, vol. 30, no. 4, pp. 1574–1584, Dec. 2015.
- [4] F. R. Alam and K. Abbaszadeh, "Magnetic field analysis in eccentric surface-mounted permanent-magnet motors using an improved conformal mapping method," *IEEE Trans. Energy Convers.*, vol. 31, no. 3, pp. 333–344, Apr. 2016.
- [5] P. B. Reddy, A. M. EL-Refaie, K.-K. Huh, J. K. Tangudu, and T. M. Jahns, "Comparison of interior and surface PM machines equipped with fractional-slot concentrated windings for hybrid traction applications," *IEEE Trans. Energy Convers.*, vol. 27, no. 3, pp. 593–602, Sep. 2012.
- [6] W. Zhao, J. Zheng, J. Wang, G. Liu, J. Zhao, and Z. Fang, "Design and analysis of a linear permanent-magnet vernier machine with improved force density," *IEEE Trans. Ind. Electron.*, vol. 63, no. 4, pp. 2072–2082, Apr. 2016.
- [7] P. Zheng *et al.*, "Investigation of a novel five-phase modular permanent-magnet in-wheel motor," *IEEE Trans. Magn.*, vol. 47, no. 10, pp. 4084–4087, Oct. 2011.
- [8] F. Parasiliti, M. Villani, S. Lucidi, and F. Rinaldi, "Finite-element-based multiobjective design optimization procedure of interior permanent magnet synchronous motors for wide constant-power region operation," *IEEE Trans. Ind. Electron.*, vol. 59, no. 6, pp. 2503–2514, Jun. 2012.
- [9] X. Lu, K. Lakshmi Varaha Iyer, K. Mukherjee, K. Ramkumar, and N. Kar, "Investigation of permanent-magnet motor drives incorporating damper bars for electrified vehicles," *IEEE Trans. Ind. Electron.*, vol. 62, no. 5, pp. 3234–3244, May 2015.
- [10] X. Liu, H. Chen, J. Zhao, and A. Belahcen, "Research on the performances and parameters of interior PMSM used for electric vehicles," *IEEE Trans. Ind. Electron.*, vol. 63, no. 6, pp. 3533–3545, Jun. 2016.
- [11] J. S. Hsu, C. W. Ayers, and C. L. Coomer, "Report on Toyota/Prius motor design and manufacturing assessment," Oak Ridge Nat. Lab., U.S. Dept. Energy, 2004.
- [12] T. A. Burruss, S. L. Campbell, and C. L. Coomer, "Evaluation of the 2010 Toyota Prius hybrid synergy drive system," Oak Ridge Nat. Lab., U.S. Dept. Energy, 2011.
- [13] R. Cao, C. Mi, and M. Cheng, "Quantitative comparison of flux-switching permanent-magnet motors with interior permanent magnet motor for EV, HEV, and PHEV applications," *IEEE Trans. Magn.*, vol. 48, no. 8, pp. 2374–2384, Aug. 2012.

- [14] J. T. Chen and Z. Q. Zhu, "Winding configurations and optimal stator and rotor pole combination of flux-switching PM brushless ac machines," *IEEE Trans. Energy Convers.*, vol. 25, no. 2, pp. 293–302, Jun. 2010.
- [15] D. G. Dorrell, A. M. Knight, L. Evans, and M. Popescu, "Analysis and design techniques applied to hybrid vehicle drive machines—assessment of alternative IPM and induction motor topologies," *IEEE Trans. Ind. Electron.*, vol. 59, no. 10, pp. 3690–3699, Oct. 2012.
- [16] Q. Chen, G. Liu, W. Zhao, M. Shao, L. Sun, and Z. Liu, "Design and comparison of two fault-tolerant interior permanent-magnet motors," *IEEE Trans. Ind. Electron.*, vol. 61, no. 12, pp. 6615–6623, Dec. 2014.
- [17] M. Kimiabeigi *et al.*, "High-performance low-cost electric motor for electric vehicles using ferrite magnets," *IEEE Trans. Ind. Electron.*, vol. 63, no. 1, pp. 113–122, Jan. 2016.
- [18] N. Bianchi and H. Mahmoud, "An analytical approach to design the PM in PMAREL motors robust toward the demagnetization," *IEEE Trans. Energy Convers.*, vol. 31, no. 2, pp. 800–809, Feb. 2016.
- [19] I. Boldea, L. Tutelea, L. Parsa, and D. Dorrell, "Automotive electric propulsion systems with reduced or no permanent magnets: An overview," *IEEE Trans. Ind. Electron.*, vol. 61, no. 10, pp. 5696–5711, Oct. 2014.
- [20] R. Vandana and B. G. Fernandes, "Design methodology for high-performance segmented rotor switched reluctance motors," *IEEE Trans. Energy Convers.*, vol. 30, no. 1, pp. 11–21, Mar. 2015.
- [21] M. Takeno *et al.*, "Test results and torque improvement of the 50-kW switched reluctance motor designed for hybrid electric vehicles," *IEEE Trans. Ind. Appl.*, vol. 48, no. 4, pp. 1327–1334, Jul./Aug. 2012.
- [22] K. Wang, Z. Q. Zhu, G. Ombach, and W. Chlebosz, "Average torque improvement of interior permanent-magnet machine using third harmonic in rotor shape," *IEEE Trans. Ind. Electron.*, vol. 61, no. 9, pp. 5047–5057, Sep. 2014.
- [23] K. Wang, Z. Q. Zhu, Y. Ren, and G. Ombach, "Torque improvement of dual three-phase permanent-magnet machine with third-harmonic current injection," *IEEE Trans. Ind. Electron.*, vol. 62, no. 11, pp. 6833–6844, Nov. 2015.
- [24] W. Zhao, F. Zhao, T. Lipo, and B. Kwon, "Optimal design of a novel v-type interior permanent magnet motor with assisted barriers for the improvement of torque characteristics," *IEEE Trans. Magn.*, vol. 50, no. 11, Nov. 2014, Art. ID 8104504.
- [25] W. Zhao, T. Lipo, and B. Kwon, "Optimal design of a novel asymmetrical rotor structure to obtain torque and efficiency improvement in surface inset pm motors," *IEEE Trans. Magn.*, vol. 51, no. 3, Mar. 2015, Art. ID 8100704.
- [26] W. Q. Chu and Z. Q. Zhu, "Investigation of torque ripple in PM synchronous machines with skewing," *IEEE Trans. Magn.*, vol. 49, no. 3, pp. 1211–1220, Mar. 2013.
- [27] I. A. A. Afinowi, Z. Q. Zhu, Y. Guan, J. C. Mipo, and P. Farah, "Electromagnetic performance of stator slot permanent magnet machines with/without stator tooth-tips and having single/double layer windings," *IEEE Trans. Magn.*, vol. 52, no. 6, Jun. 2016, Art. ID 8103410.
- [28] N. Bianchi and S. Bolognani, "Reducing torque ripple in PM synchronous motors," in *Proc. Int. Conf. Elect. Mach.*, Helsinki, Finland, Aug. 28–30, 2000, pp. 1222–1226.
- [29] G. Liu, X. Du, W. Zhao, and Q. Chen, "Reduction of torque ripple in inset permanent magnet synchronous motor by magnets shifting," *IEEE Trans. Magn.*, vol. 53, no. 2, Feb. 2017, Art. ID 8100713.
- [30] T. Sun, J. Wang, and X. Chen, "Maximum torque per ampere (MTPA) control for interior permanent magnet synchronous machine drives based on virtual signal injection," *IEEE Trans. Power Electron.*, vol. 30, no. 9, pp. 5036–5045, Sep. 2015.



**Guohai Liu** (M'07–SM'15) received the B.Sc. degree from Jiangsu University, Zhenjiang, China, in 1985, and the M.Sc. and Ph.D. degrees from Southeast University, Nanjing, China, in 1988 and 2002, respectively, in electrical engineering and control engineering.

He has been with Jiangsu University since 1988, where he is currently a Professor, the Dean of the School of Electrical Information Engineering. From 2003 to 2004, he was a Visiting Professor with the Department of Electronic and Electrical Engineering, University of Sheffield, Sheffield, U.K. His teaching and research interests include electrical machines, motor drives for electric vehicles and intelligent control. He has authored or coauthored over 200 technical papers and four textbooks, and holds 35 patents in these areas.



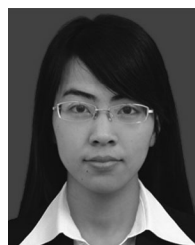
**Gaohong Xu** received the B.Sc. degree in electrical engineering and automation and the M.Sc. degree in power electronics and power drives in 2009 and 2012, respectively, from Jiangsu University, Zhenjiang, China, where she is currently working toward the Ph.D. degree.

Her current research interests include computation of electromagnetic fields for permanent-magnet machine and electric machine design.



**Wenxiang Zhao** (M'08–SM'14) received the B.Sc. and M.Sc. degrees in electrical engineering from Jiangsu University, Zhenjiang, China, in 1999 and 2003, respectively, and the Ph.D. degree in electrical engineering from Southeast University, Nanjing, China, in 2010.

He has been with Jiangsu University since 2003, where he is currently a Professor with the School of Electrical Information Engineering. From 2008 to 2009, he was a Research Assistant with the Department of Electrical and Electronic Engineering, University of Hong Kong, Hong Kong. From 2013 to 2014, he was a Visiting Professor with the Department of Electronic and Electrical Engineering, University of Sheffield, Sheffield, U.K. His current research interests include electric machine design, modeling, fault analysis, and intelligent control. He has authored and coauthored more than 130 technical papers in these areas.



**Xinxin Du** received the B.Sc. degree in electrical engineering and automation from Jiangsu University, Zhenjiang, China, in 2015, where she is currently working toward the M.Sc. degree in electrical engineering.

Her current research interests include design of permanent-magnet machine.



**Qian Chen** (M'16) received the B.Sc. and Ph.D. degrees from Jiangsu University, Zhenjiang, China, in 2009 and 2015, respectively, in electrical engineering and control engineering.

He has been with Jiangsu University since 2015, where he is currently a Lecturer in the School of Electrical Information Engineering. His current research interests include electric machine design, modeling, fault analysis, and intelligent control.